J. Fluid Mech. (2015), *vol.* 779, *pp.* 181–196.
doi:10.1017/jfm.2015.425

Elastohydrodynamics of a sliding, spinning and sedimenting cylinder near a soft wall

Thomas Salez[1,2] **and L. Mahadevan**[1,†]

[1]School of Engineering and Applied Sciences and Department of Physics, Harvard University, Cambridge, MA 02138, USA

[2]PCT Lab, UMR CNRS 7083 Gulliver, ESPCI ParisTech, PSL Research University, 75005 Paris, France

(Received 18 January 2015; revised 3 June 2015; accepted 20 July 2015)

We consider the motion of a fluid-immersed negatively buoyant particle in the vicinity of a thin compressible elastic wall, a situation that arises in a variety of technological and natural settings. We use scaling arguments to establish different regimes of sliding, and complement these estimates using thin-film lubrication dynamics to determine an asymptotic theory for the sedimentation, sliding and spinning motions of a cylinder. The resulting theory takes the form of three coupled nonlinear singular-differential equations. Numerical integration of the resulting equations confirms our scaling relations and further yields a range of unexpected behaviours. Despite the low-Reynolds-number feature of the flow, we demonstrate that the particle can spontaneously oscillate when sliding, can generate lift via a Magnus-like effect, can undergo a spin-induced reversal effect and also shows an unusual sedimentation singularity. Our description also allows us to address a sedimentation–sliding transition that can lead to the particle coasting over very long distances, similar to certain geophysical phenomena. Finally, we show that a small modification of our theory allows us to generalize the results to account for additional effects such as wall poroelasticity.

Key words: low-Reynolds-number flows, lubrication theory, particle/fluid flows

1. Introduction

The sedimentation of a heavy solid in a fluid has been studied thoroughly, as the dynamics of settling and sliding is relevant to a broad class of phenomena across many orders of magnitude, ranging from landslides (Campbell 1989), earthquakes (Ma *et al.* 2003) and avalanches (Glenne 1987) to the lubrication of cartilaginous joints (Grodzinsky, Lipshitz & Glimcher 1978; Mow, Holmes & Lai 1984; Mow & Guo 2002) and the motion of cells in a microfluidic channel (Byun *et al.* 2013) or in a blood vessel (Goldsmith 1971). Following the now classical studies of the dynamics of a particle near a rigid wall (Brenner 1962; Goldman, Cox & Brenner 1967*a*,*b*; Jeffrey & Onishi 1981), additional effects such as the influence of the boundary conditions (Hocking 1973), and their role on drag (Trahan & Hussey 1985), viscometry (Wehbeh, Ui & Hussey 1993) and bouncing (Gondret *et al.* 1999) have been accounted for.

† Email address for correspondence: lm@seas.harvard.edu

Recently, the motion of wedge-like objects down an incline (Cawthorn & Balmforth 2010), as well as the effects of elasticity in such contexts as granular impact (Davis, Serayssol & Hinch 1986), polymer-bearing contacts (Sekimoto & Leibler 1993), solvent permeation in gels (Sekimoto & Rabin 1994), soft lubrication (Skotheim & Mahadevan 2004*a*, 2005), transient effects in displacement-controlled systems (Weekley, Waters & Jensen 2006), settling on soft and poroelastic beds (Balmforth, Cawthorn & Craster 2010; Gopinath & Mahadevan 2011), adhesive walls (Mani, Gopinath & Mahadevan 2012) and self-similar contact (Snoeijer, Eggers & Venner 2013) have also been addressed. In all of these phenomena, the minimal model of motion relates to that of a solid object immersed in a viscous fluid in the vicinity of a soft elastic or poroelastic wall.

Perhaps surprisingly then, the general theory for the free motion of a rigid solid close to a soft incline – which has through its degrees of freedom the ability to simultaneously sediment, slide and spin – does not seem to have been considered. These modes naturally arise in several applications such as particle capture and joint lubrication, and have analogues in certain geophysical phenomena. Here, we study this problem in a minimal setting and describe the essential scalings and qualitative features, develop a soft lubrication theory that complements these scaling ideas and solve the resulting equations numerically to characterize the broad range of possible behaviours.

2. Mathematical model and scaling analysis

We consider the 2D system depicted in figure 1, which consists of the free gravitational fall of a long cylinder of radius r, density ρ, mass (per unit length) $m = \pi r^2 \rho$ and buoyant mass $m^* = \pi r^2 \rho^* = \pi r^2 (\rho - \rho_{fluid}) > 0$, where ρ_{fluid} is the density of the neighbouring fluid of viscosity η. We assume that the motion of the cylinder occurs in the vicinity of a wall that is inclined at an angle $\alpha \in [0, \pi/2]$ with respect to the horizontal direction and coated with a soft elastic layer of thickness h_s, and Lamé coefficients μ and λ. We denote by $\delta_s(x, t)$ the deformation of the fluid–wall interface. We note that a positive indentation of the compressible elastic wall corresponds to a negative value of δ_s. The system is assumed to be invariant along y, i.e. we limit ourselves to planar motions wherein the cylinder has three degrees of freedom: the gap $\delta(t)$ between the cylinder and the undeformed wall along z, the tangential coordinate $x_G(t)$ of the cylinder axis along x and the angle $\theta(t)$ through which the cylinder has rotated.

We further assume that the cylinder starts its motion at time $t = 0$, with $\delta(0) = \delta_0 = \epsilon r \ll r$, and possibly non-zero initial translational and angular velocity. Due to this scale separation, we are in the lubrication regime (Batchelor 1967), where the fluid viscous shear stresses are small relative to the flow-induced pressure $p(x, t)$. We note that there is an additional hydrostatic contribution to the pressure through the buoyancy of the cylinder, which we will consider later. Thus, $p(x, t)$ contains only the flow contribution, which itself vanishes far from the contact zone as $x \to \pm\infty$. The tangential extent $l(t) \gg \delta(t)$ of the flow-induced pressure disturbance scales as $l(t) \sim \sqrt{r\delta(t)} \ll r$, so that as for Hertzian contact (Johnson 1985), we can assume a parabolic shape of the deformed interface, and the total gap profile may be written as

$$h(x, t) = \delta(t) - \delta_s(x, t) + \frac{[x - x_G(t)]^2}{2r}. \tag{2.1}$$

The thin soft compressible wall may also be treated via a lubrication-like theory for elastic deformations if $h_s \ll l(t)$, so that the algebraic displacement $\delta_s(x, t)$ of the

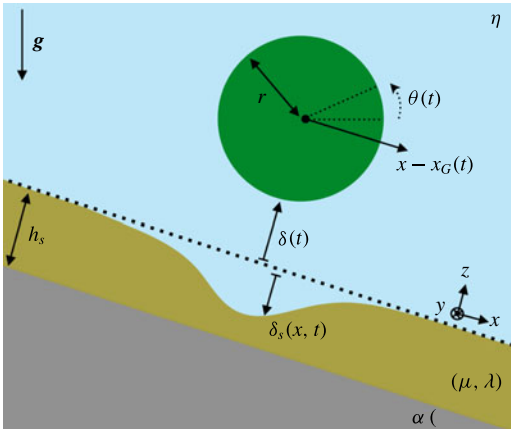

FIGURE 1. (Colour online) Schematic of the system. A negatively buoyant cylinder (green) falls down under the influence of gravity $\boldsymbol{g}$, inside a viscous fluid (blue), in the vicinity of a thin soft wall (brown). The ensemble lies atop a tilted infinitely rigid support (grey).

fluid–wall interface is simply obtained from the linear elastic response to the local flow-induced pressure disturbance (Skotheim & Mahadevan 2004*a*, 2005):

$$\delta_s(x, t) = -\frac{h_s p(x, t)}{2\mu + \lambda}. \tag{2.2}$$

We note that when δ is too small, the condition $h_s \ll \sqrt{r\delta}$ is not satisfied. Nevertheless, if for instance $h_s \sim \delta_0$, this is a valid assumption since $\delta \sim \delta_0 \ll r$.

To characterize the motion of the cylinder near the inclined thin soft wall, we need to calculate the fluid drag force created by the flow-induced pressure field in the contact zone, which is driven by the tangential fluid velocity $u(x, z, t)$ along x. We non-dimensionalize the problem using the following choices: $z = Zr\epsilon$, $h = Hr\epsilon$, $\delta = \Delta r\epsilon$, $x = Xr\sqrt{2\epsilon}$, $x_G = X_G r\sqrt{2\epsilon}$, $\theta = \Theta\sqrt{2\epsilon}$, $t = Tr\sqrt{2\epsilon}/c$, $u = Uc$ and $p = P\eta c\sqrt{2}/(r\epsilon^{3/2})$, where we have introduced a free fall velocity scale $c = \sqrt{2gr\rho^*/\rho}$ and the dimensionless parameter

$$\xi = \frac{3\sqrt{2}\,\eta}{r^{3/2}\epsilon\sqrt{\rho\rho^* g}}. \tag{2.3}$$

This parameter measures the ratio of the free fall time $\sqrt{\rho r\epsilon/(\rho^* g)}$ and the typical lubrication damping time $m\epsilon^{3/2}/\eta$ over which the inertia of the cylinder vanishes. In fact, for a cylinder falling towards a rigid wall, the lubrication drag force (per unit length) exerted in the contact zone reads $\sim -\eta\dot{\delta}/\epsilon^{3/2}$ (Jeffrey & Onishi 1981). The typical decay time of the cylinder inertia can thus be estimated by balancing this damping force and the inertia (per unit length) $m\ddot{\delta}$, which leads to the above time scale.

With these definitions, the dimensionless gap profile given by (2.1) becomes

$$H(X, T) = \Delta(T) + [X - X_G(T)]^2 + \kappa P(X, T), \tag{2.4}$$

where the dimensionless compliance is

$$\kappa = \frac{2h_s\eta\sqrt{g\rho^*}}{r^{3/2}\epsilon^{5/2}(2\mu + \lambda)\sqrt{\rho}}. \tag{2.5}$$

To remain in the linearly elastic regime for the wall deformation, we assume that $\kappa \ll 1$.

Before delving into a detailed theory, we first derive some scaling relations for the sliding dynamics of the cylinder. For steady motions, the analysis of Sekimoto & Leibler (1993) and Skotheim & Mahadevan (2004*a*, 2005) shows that one non-trivial effect of the soft substrate is to induce a positive elastohydrodynamic pressure $\sim\eta^2\dot{x}_G^2 r h_s/(\mu\delta^4)$ in the contact zone, when the particle is translated uniformly along the wall at speed $\dot{x}_G$ while being at a constant distance δ. In the present 2D-like case of a free cylinder, when that pressure is integrated once along the contact length $l \sim \sqrt{r\delta}$, this leads to a net positive elastohydrodynamic lift force (per unit length) $\sim\eta^2\dot{x}_G^2 r^{3/2} h_s/(\mu\delta^{7/2})$ that tends to repel the sliding particle away from the soft wall. Since the force of gravity (per unit length) $\sim\rho^* g r^2 \cos\alpha$ tends to bring it back towards the wall, balancing the two forces allows one to predict a sliding height as a function of the speed $\dot{x}_G$, given by

$$\delta_{eq} \sim \left(\frac{h_s \eta^2 \dot{x}_G^2}{\mu\sqrt{r}\rho^* g\cos\alpha}\right)^{2/7}. \tag{2.6}$$

When the sliding velocity $\dot{x}_G$ does not vary much – as is often the case on short time scales when the damping in the normal direction z is much stronger than that in the tangential direction x – this represents a stable equilibrium gap thickness. A small perturbation about this equilibrium position suggests that the cylinder will oscillate with frequency $\sim\sqrt{\rho^* g\cos\alpha/(\rho\delta_{eq})}$, even though the lubrication viscous damping will cause these inertial oscillations to decay over a typical time $\sim(\delta_{eq}/r)^{3/2} m/\eta$, as already introduced above.

Finally, after a transient evolution along the tilted wall, we expect the cylinder to reach a long-term steady-state sliding regime characterized by a terminal velocity u_∞ and a constant gap thickness δ_∞. Leaving aside the conditions of existence of this scenario for now, we can already describe the properties of this regime using simple arguments. Along z, the gravity-versus-lift force balance leads to (2.6) above, with $\dot{x}_G = u_\infty$ and $\delta_{eq} = \delta_\infty$. The second equation we need comes from the power balance in the direction of sliding motion x. The power (per unit length) $\sim u_\infty \rho^* g r^2 \sin\alpha$ generated by the gravitational driving is entirely dissipated in the contact zone through the viscous damping power $\sim\eta(u_\infty/\delta_\infty)^2 l\delta_\infty \sim \eta u_\infty^2\sqrt{r/\delta_\infty}$. This leads to the expressions for the steady gap and terminal velocity, given by

$$\delta_\infty \sim \frac{\rho^{*2/5} g^{2/5} r h_s^{2/5} \sin^{4/5}\alpha}{\mu^{2/5}\cos^{2/5}\alpha}, \quad u_\infty \sim \frac{\rho^{*6/5} g^{6/5} r^2 h_s^{1/5}\sin^{7/5}\alpha}{\eta\mu^{1/5}\cos^{1/5}\alpha}. \tag{2.7a,b}$$

With these scaling relationships in place, we now aim at constructing a detailed soft lubrication theory that goes beyond these arguments and, as we will see, introduces new phenomena as well.

3. Soft lubrication theory

In the thin-gap limit, the governing Stokes equations for incompressible viscous flow are given in scaled form by (Reynolds 1886; Batchelor 1967; Oron, Davis & Bankoff 1997)

$$U_{ZZ} = P_X, \tag{3.1}$$

together with no-slip boundary conditions, $U(X, Z=-\kappa P, T)=0$ and $U(X, Z=H-\kappa P, T)=\dot{X}_G+\dot{\Theta}$. Solving (3.1) with the above boundary conditions, and invoking the condition of volume conservation,

$$\partial_T H+\partial_X \int_{-\kappa P}^{H-\kappa P} \mathrm{d}Z\ U=0, \tag{3.2}$$

yields the following equation for the evolution of the gap:

$$12\dot{\Delta}-24\,(X-X_G)\,\dot{X}_G+12\kappa P_T=\left[H^3 P_X-6\left(\dot{X}_G+\dot{\Theta}\right)H\right]_X. \tag{3.3}$$

The solution of this equation allows us to evaluate the total pressure-induced drag exerted on the cylinder, through

$$\boldsymbol{D}_p\approx\int_{-\infty}^{\infty}\mathrm{d}X\,P\ \boldsymbol{e}_z-\sqrt{2\epsilon}\int_{-\infty}^{\infty}\mathrm{d}X\ (X-X_G)\,P\ \boldsymbol{e}_x, \tag{3.4}$$

where we have used the fact that the normal vector to the cylinder surface is $\boldsymbol{n}\approx\boldsymbol{e}_z-((x-x_G)/r)\boldsymbol{e}_x$. Similarly, the shear drag force exerted on the cylinder along the $\boldsymbol{e}_x$ axis is given by

$$D_{\sigma,\parallel}=-\sqrt{\frac{\epsilon}{2}}\int_{-\infty}^{\infty}\mathrm{d}X\,U_Z|_{Z=H-\kappa P}. \tag{3.5}$$

When the dimensionless compliance is assumed to satisfy $\kappa\ll 1$, we may employ perturbation theory in this parameter (Skotheim & Mahadevan 2004*a*, 2005), using the following expansion for the pressure: $P=P^{(0)}+\kappa P^{(1)}$, where $P^{(0)}|_{X\to\pm\infty}=P^{(1)}|_{X\to\pm\infty}=0$. As detailed in Appendix A and B, integrating (3.3) to first order in κ, and using (3.4) and (3.5), leads to the following expressions for the perpendicular drag along $\boldsymbol{e}_z$ and the two parallel components along $\boldsymbol{e}_x$:

$$\left.\begin{aligned}
D_{p,\perp}&=-\frac{3\pi}{2}\frac{\dot{\Delta}}{\Delta^{3/2}}+\kappa\left[\frac{45\pi\ddot{\Delta}}{16\Delta^{7/2}}-\frac{63\pi\dot{\Delta}^2}{8\Delta^{9/2}}+\frac{3\pi\left(\dot{\Theta}-\dot{X}_G\right)^2}{8\Delta^{7/2}}\right],\\
D_{p,\parallel}&=\pi\sqrt{2\epsilon}\ \frac{\dot{\Theta}-\dot{X}_G}{\sqrt{\Delta}}+\kappa\sqrt{\frac{\epsilon}{2}}\left[\frac{23\pi\dot{\Delta}\left(\dot{\Theta}-\dot{X}_G\right)}{8\Delta^{7/2}}+\frac{\pi\left(\ddot{X}_G-\ddot{\Theta}\right)}{2\Delta^{5/2}}\right],\\
D_{\sigma,\parallel}&=-\pi\sqrt{2\epsilon}\frac{\dot{\Theta}}{\sqrt{\Delta}}+\kappa\sqrt{\frac{\epsilon}{2}}\left[\frac{\pi\left(\ddot{\Theta}-\ddot{X}_G\right)}{4\Delta^{5/2}}+\frac{\pi\dot{\Delta}\dot{X}_G}{2\Delta^{7/2}}-\frac{19\pi\dot{\Delta}\dot{\Theta}}{8\Delta^{7/2}}\right].
\end{aligned}\right\} \tag{3.6}$$

We stress that we have neglected the forces acting outside the contact zone, consistent with the lubrication approximation. To justify this choice, let us first consider the sedimentation motion towards the rigid wall. The drag force (per unit length) exerted on a cylinder in a bulk fluid scales as $d_{bulk}\sim\eta\dot{\delta}$ (Brenner 1962). According to (3.6), the pressure-induced lubrication drag force (per unit length) reads, in real variables, $d_{p,\perp}=2c\eta D_{p,\perp}/\epsilon\sim\eta\dot{\delta}(r/\delta)^{3/2}$ (Jeffrey & Onishi 1981). Since $\delta\ll r$ in the lubrication approximation, one can safely neglect the bulk drag relative to the lubrication one acting in the contact zone. Similarly, according to (3.6), for the tangential motion along a rigid wall, the pressure-induced drag scales as $d_{p,\parallel}=2c\eta D_{p,\parallel}/\epsilon\sim\eta\dot{x}_G\sqrt{r/\delta}$ (Jeffrey & Onishi 1981), which – despite being smaller than $d_{p,\perp}$ – is once again larger than d_{bulk} in the lubrication approximation. One can

thus safely neglect the bulk drag relative to the lubrication drag for the tangential degree of freedom as well. Since the shear-induced drag is of the same order and symmetry as the tangential pressure-induced drag, the previous conclusion extends immediately to the rotational degree of freedom. We note that the argument above assumes a rigid wall, since the fluid lubrication order is not modified by the softness of the wall. As an illustration of this statement, all the softness-induced terms – the ones proportional to the independent compliance parameter κ in (3.6) – have the same order in ϵ as the corresponding terms for the rigid wall.

We also note that it may not be satisfactory at first sight to obtain an acceleration-dependent drag, even as a first-order correction, as it means that at time $T = 0$, when there is no flow, there is a pressure field that deforms the wall. To understand this, we note that the origin of this behaviour is to be found in the P_T term in (3.3), since $P \propto \dot{\Delta}$ due to the Stokes equation. In our analysis, we have neglected the linearized inertia of the fluid, $\rho_{fluid}\partial_t u$, but at very short times this term becomes dominant and resolves this apparent paradox.

Knowing the dominant elastohydrodynamic drag forces acting on the cylinder, we now use the balance of linear and angular momentum (see Appendix A and B) to write down the coupled nonlinear differential equations for the translational and rotational motions of the cylinder, as it sediments, slides and rolls down the incline:

$$\left.\begin{aligned}
\ddot{\Delta} &= -\xi\frac{\dot{\Delta}}{\Delta^{3/2}} - \frac{\kappa\xi}{4}\left[21\frac{\dot{\Delta}^2}{\Delta^{9/2}} - \frac{\left(\dot{\Theta}-\dot{X}_G\right)^2}{\Delta^{7/2}} - \frac{15}{2}\frac{\ddot{\Delta}}{\Delta^{7/2}}\right] - \cos\alpha,\\
\ddot{X}_G &= -\frac{2\epsilon\xi}{3}\frac{\dot{X}_G}{\sqrt{\Delta}} - \frac{\kappa\epsilon\xi}{6}\left[\frac{19}{4}\frac{\dot{\Delta}\dot{X}_G}{\Delta^{7/2}} - \frac{\dot{\Delta}\dot{\Theta}}{\Delta^{7/2}} + \frac{1}{2}\frac{\ddot{\Theta}-\ddot{X}_G}{\Delta^{5/2}}\right] + \sqrt{\frac{\epsilon}{2}}\sin\alpha,\\
\ddot{\Theta} &= -\frac{4\epsilon\xi}{3}\frac{\dot{\Theta}}{\sqrt{\Delta}} - \frac{\kappa\epsilon\xi}{3}\left[\frac{19}{4}\frac{\dot{\Delta}\dot{\Theta}}{\Delta^{7/2}} - \frac{\dot{\Delta}\dot{X}_G}{\Delta^{7/2}} + \frac{1}{2}\frac{\ddot{X}_G-\ddot{\Theta}}{\Delta^{5/2}}\right].
\end{aligned}\right\} \tag{3.7}$$

We note that the lubrication pressure-induced torque vanishes since the corresponding forces act along the radii of the cylinder. Interestingly, this would not be the case for the opposite case of a soft cylinder – which will deform asymmetrically – near a rigid wall, thus breaking a once well-admitted symmetry between the two dual systems in elasticity (Johnson 1985).

We see that particle inertia plays a central role in (3.7), even though we have neglected fluid inertia. To justify this assumption, let us consider for instance an x translation of the cylinder along the rigid wall, at typical speed c and distance δ_0 from the wall. In the Navier–Stokes equation, the local fluid inertia term reads $\rho_{fluid}\partial_t u \sim \rho_{fluid}c/\tau$, where $\tau \sim l/c$ is the typical time scale of the flow at speed c, and $l \sim \sqrt{r\delta_0}$ is the length of the contact zone along x. Similarly, the convective inertia term reads $\rho_{fluid}u\partial_x u \sim \rho_{fluid}c^2/l \sim \rho_{fluid}c/\tau$. On the other hand, the viscous term in the Navier–Stokes equation reads $\eta\partial_{zz}^2 u \sim \eta c/\delta_0^2$. The ratio of inertia over viscous terms thus reads $\sim Re\,\epsilon \sim Re\,\delta_0/r$, where the Reynolds number is given by $Re = \rho_{fluid}lc/\eta$. As for the particle inertia, following Newton's law, we note that it scales as $\sim\rho r^2 l/\tau^2$. According to our (3.6), for the tangential motion along the rigid wall, the pressure-induced force (per unit length) scales as $d_{p,\parallel} = 2c\eta D_{p,\parallel}/\epsilon \sim \eta c/\sqrt{\epsilon}$ (Jeffrey & Onishi 1981), in real variables. The ratio of particle inertia and fluid viscosity thus reads $\sim(\rho/\rho_{fluid})Re/\sqrt{\epsilon}$, which is much larger than the ratio of fluid inertia and fluid viscosity – due to the lubrication parameter $\epsilon \ll 1$ – even in the case when the densities are matched. Thus, we see that even if fluid inertia plays a role

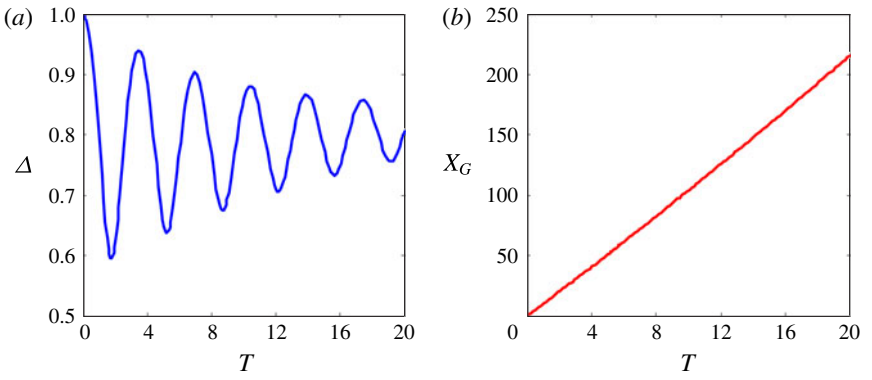

FIGURE 2. (Colour online) Oscillations: when a cylinder is released close to an inclined wall with a non-zero tangential velocity, it spontaneously oscillates about the stable sliding height; however, with time, these oscillations eventually decay. These results follow from the numerical solution of (3.7), for $\alpha = \pi/4$, $\xi = 0.1$, $\kappa = 0.1$, $\epsilon = 0.1$, $\Delta(0) = 1$, $X_G(0) = \dot{\Delta}(0) = \dot{\Theta}(0) = 0$ and $\dot{X}_G(0) = 10$.

on short time scales, there is a range of parameters over which it is negligible while particle inertia is still important. This conclusion remains valid even in the presence of the additional compliance parameter κ describing the wall softness.

4. Behaviour of solutions

The elastohydrodynamic drag terms on the right-hand sides of (3.7) trigger an interesting zoology of solutions, which we now turn to. The solutions are governed by four dimensionless control parameters corresponding to a ratio ξ of viscous damping over gravitational driving, an incline angle α, a scaled wall compliance $\kappa \ll 1$ and a scaled lubrication gap $\epsilon \ll 1$. In addition, there are three relevant initial conditions, $\dot{\Delta}(0)$, $\dot{X}_G(0)$ and $\dot{\Theta}(0)$, since $\Delta(0) = 1$ by virtue of our choice of the dimensionless variable $\Delta = \delta/\delta_0$, while all the initial tangential positions $X_G(0)$ and initial angles $\Theta(0)$ are equivalent. Below, we give a brief flavour of some of the unexpected behaviours of the system with the aim of sketching the diversity of solutions, potentially valid for a variety of similar systems and experiments, rather than building a complete phase diagram for this 2D case.

4.1. *Zoology*

In figure 2, we show that when the cylinder is released along a steep incline, it slides along it uniformly even as it spontaneously oscillates, although these oscillations are damped. Indeed, the envelope decays over a dimensionless time that is consistent with our earlier scaling estimate: $\Delta_{eq}^{3/2}/\xi \sim 6.4$ (in dimensionless form) for the parameters of figure 2. Similarly, the equilibrium height can be calculated by balancing gravity $\cos\alpha$ and the elastohydrodynamic lift $\kappa\xi\dot{X}_G^2/(4\Delta^{7/2})$ in the first line of (3.7), to yield

$$\Delta_{eq} = \frac{1}{2^{4/7}} \left(\frac{\kappa \xi \dot{X}_G^2}{\cos\alpha} \right)^{2/7}, \tag{4.1}$$

consistent with the dimensional scaling form given in (2.6). For the parameters in figure 2, one obtains $\Delta_{eq} \approx 0.74$, which is close to the observed average value of

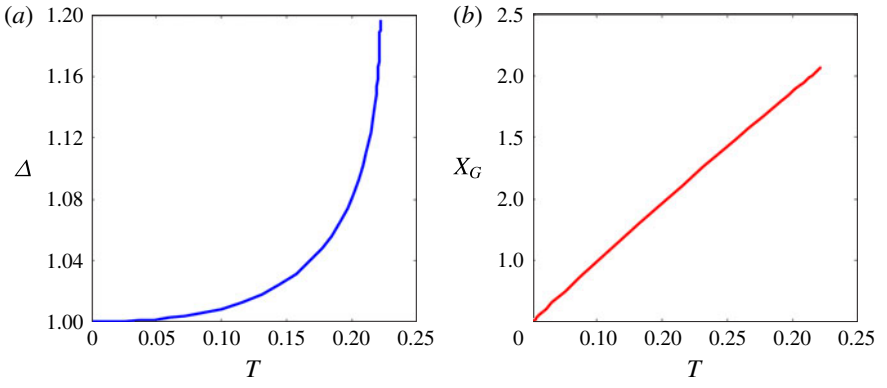

FIGURE 3. (Colour online) Magnus-like effect: when the cylinder is released close to the horizontal elastic wall with a non-zero angular velocity, it lifts off. These results follow from the numerical solution of (3.7), for $\alpha = 0$, $\xi = 10$, $\kappa = 0.1$, $\epsilon = 0.1$, $\Delta(0) = 1$, $X_G(0) = \dot{\Delta}(0) = 0$ and $\dot{X}_G(0) = \dot{\Theta}(0) = 10$. If we replace the last condition by $\dot{\Theta}(0) = 0$, then Δ diminishes.

~ 0.79 seen in figure 2(*a*); the slight difference is due to the weak influence of other terms in (3.7).

In figure 3, we show another peculiar effect associated with the case when the cylinder is started with an initial spin. As seen, it can lift off the soft wall via a Magnus-like effect (Dupeux *et al.* 2011) even as it slides along a horizontal wall. This effect is due to the fluid shear induced by rotation which leads to an increased hydrodynamic pressure, which deforms the wall and thence leads to a normal force.

Next, we turn to examine the equations when the effective mass of the particle vanishes. Indeed, since we kept both the cylinder inertia and the acceleration drag, as explained above, those two second-derivative terms may cancel each other. This singularity leads to a vanishing effective mass and thus a diverging acceleration $\ddot{\Delta}$, and occurs at the three critical heights:

$$\Delta_{c1} = \left(\frac{15\kappa\xi}{8}\right)^{2/7}, \tag{4.2}$$

$$\Delta_{c2} = \left(\frac{\epsilon\kappa\xi}{12}\right)^{2/5}, \tag{4.3}$$

$$\Delta_{c3} = \left(\frac{\epsilon\kappa\xi}{6}\right)^{2/5}. \tag{4.4}$$

In figure 4, we show the evolution of the height when a relatively heavy cylinder is released above a horizontal soft wall, by following Δ which is related to but is not exactly a cylinder–wall distance, since there is an additional $\kappa P(X_G, T)$ term according to (2.4). However, this additional term can be computed from (A 4) and the solutions of (3.7), if needed. We see that the particle sediments at an enhanced rate relative to the case when the soft wall is replaced by a rigid wall, corresponding to $\kappa = 0$. This is due to the fact that when the cylinder reaches the largest critical height $\Delta_{c1} < 1$ of (4.2), the vanishing effective inertial mass leads to an infinite acceleration. This unphysical effect is regularized when one takes into account fluid inertia, leading to a

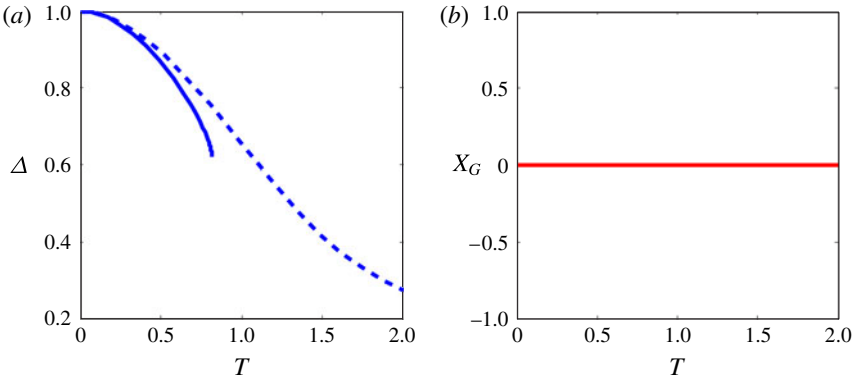

FIGURE 4. (Colour online) Enhanced sedimentation: when the cylinder is allowed to fall freely vertically towards the horizontal elastic wall, it sediments faster than if the wall is rigid. These results follow from the numerical solutions of (3.7), for $\alpha = 0$, $\xi = 1$, $\epsilon = 0.1$, $\Delta(0) = 1$ and $X_G(0) = \dot{\Delta}(0) = \dot{X}_G(0) = \dot{\Theta}(0) = 0$. The dashed line corresponds to the case of a rigid wall, with $\kappa = 0$, showing that Δ decreases gradually, while the solid line corresponds to sedimentation towards a soft wall, with $\kappa = 0.1$, where the cylinder abruptly crashes downwards after sedimenting at a rate faster than towards a rigid wall. Panel (*b*) shows that the horizontal position of the cylinder does not vary at all during sedimentation (the simulation is extended to $T = 2$ corresponding to the case of sedimentation towards a rigid wall).

smoothed out temporal profile of sedimentation. Nonetheless, as explained above, the temporal cutoff associated with fluid inertia is assumed to correspond to time scales smaller than the ones associated with the motion of the cylinder, which means that, even if finite, $\ddot{\Delta}$ may be large and the behaviour still very sharp. Finally, we note that when $\Delta_{c1} > 1$ and $\dot{\Delta} < 0$, the singularity may instead occur at $\Delta_{c3} > \Delta_{c2}$.

We now use our results to characterize the sedimentation–sliding transition for a cylinder falling down an incline. Equation (4.1) suggests that the cylinder can stably slide at a dimensionless height Δ_{eq}. On the other hand, if for instance $\Delta_{c1} < 1$ in (4.2), Δ_{c1} fixes the relevant singular sedimentation height that may be encountered during the fall of the cylinder, as illustrated in figure 4. The balance of these two dimensionless heights yields the threshold tangential velocity U_c above which sliding becomes possible:

$$U_c = \sqrt{\tfrac{15}{2}}\sqrt{\cos\alpha}. \tag{4.5}$$

In fact, if $\Delta_{eq} < \Delta_{c1} < 1$, and thus $\dot{X}_G < U_c$, the singular sedimentation height Δ_{c1} is reached before the sliding height Δ_{eq}, and one typically gets sedimentation. If, in contrast, $\Delta_{eq} > \Delta_{c1}$, and thus $\dot{X}_G > U_c$, the sliding height Δ_{eq} is reached before the singular sedimentation height Δ_{c1}, and one typically gets sliding. This transition is illustrated in figure 5, for two given sets of dimensionless parameters and initial conditions. For instance, with a metre-sized body, this reasonably corresponds to an $\sim$1 m s^{-1} threshold velocity. We note that, although the presence of an elastic wall is crucial in the underlying mechanism, the elastohydrodynamic details do not appear in this purely gravitational expression.

We conclude our tour of the zoology of solutions by noting that when a relatively heavy cylinder is released with spin and tangential velocity, it can reverse its direction

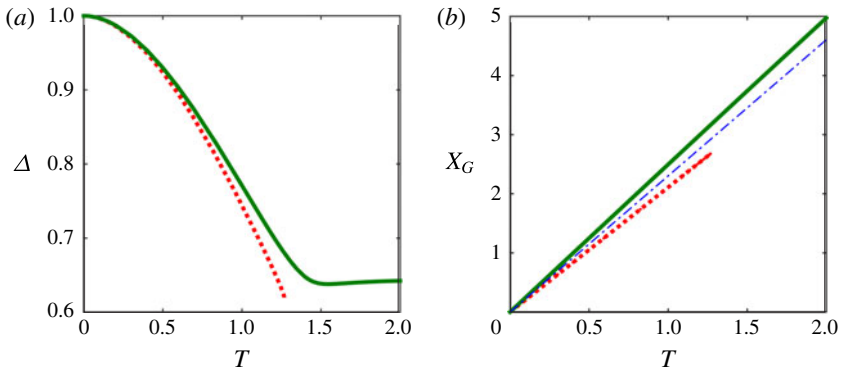

FIGURE 5. (Colour online) Sedimentation–sliding transition, observed when the cylinder is released close to the inclined elastic wall with the threshold tangential velocity given by (4.5). The results follow from the numerical solution of (3.7), for $\alpha = \pi/4$, $\xi = 1$, $\kappa = 0.1$, $\epsilon = 0.1$, $\Delta(0) = 1$, $X_G(0) = \dot{\Delta}(0) = \dot{\Theta}(0) = 0$, $\dot{X}_G(0) = 2.1$ (red dots) and $\dot{X}_G(0) = 2.5$ (green lines). For these parameters, $U_c \approx 2.30$ (blue dash-dotted line), as obtained from (4.5).

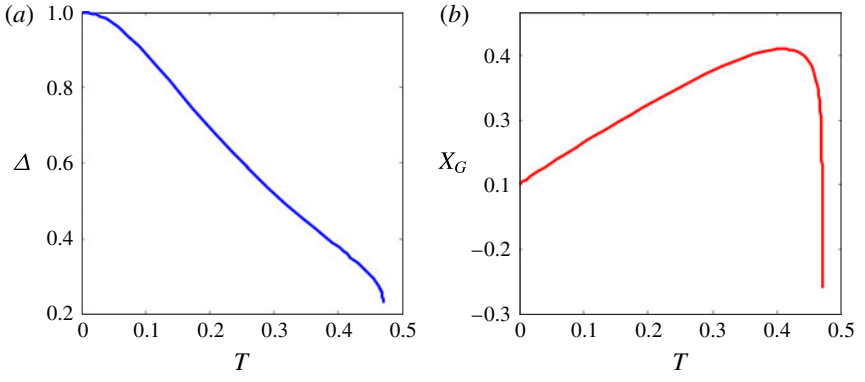

FIGURE 6. (Colour online) Spin-induced reversal: when the cylinder is released close to the horizontal elastic wall with non-zero tangential and rotational velocities, it can return backwards. These results follow from the numerical solution of (3.7), for $\alpha = 0$, $\xi = 10$, $\kappa = 0.1$, $\epsilon = 0.1$, $\Delta(0) = 1$, $X_G(0) = \dot{\Delta}(0) = 0$, $\dot{X}_G(0) = 1$ and $\dot{\Theta}(0) = 10$.

of motion and return backwards along the soft wall, as shown in figure 6. This effect can be understood by noting that the second equation in (3.7) characterizes the dynamics of sliding. Thus, when $\dot{\Delta} < 0$, a large enough positive spin velocity suffices to bring about a reversal in the tangential acceleration.

4.2. *Long-term steady sliding*

Once initiated and stabilized, the sliding motion eventually reaches a long-term steady state, with a terminal velocity that reads

$$U_\infty = \frac{3^{7/5}}{2^{5/2}} \frac{\kappa^{1/5} \sin^{7/5} \alpha}{\xi^{6/5} \epsilon^{7/10} \cos^{1/5} \alpha}, \tag{4.6}$$

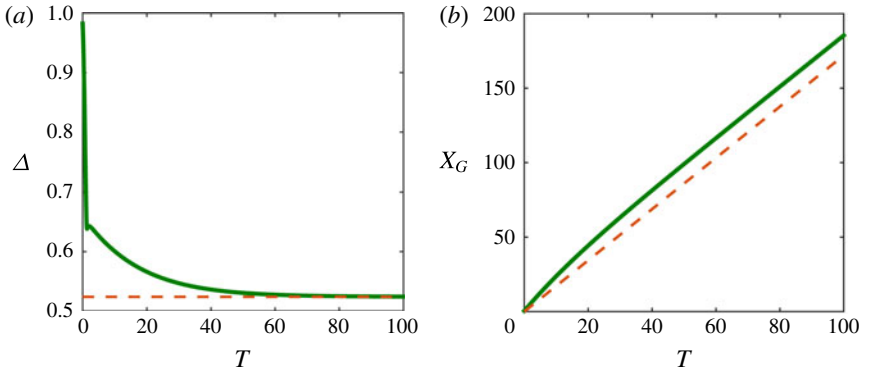

FIGURE 7. (Colour online) Convergence to the long-term sliding steady state, observed when the cylinder is released close to the inclined elastic wall with an initial tangential velocity greater than the threshold velocity given by (4.5). The results follow from the numerical solution of (3.7), for $\alpha = \pi/4$, $\xi = 1$, $\kappa = 0.1$, $\epsilon = 0.1$, $\Delta(0) = 1$, $X_G(0) = \dot{\Delta}(0) = \dot{\Theta}(0) = 0$ and $\dot{X}_G(0) = 2.5$ (green lines). For those parameters, the terminal height and velocity of the sliding steady state are given by $\Delta_\infty \approx 0.524$ and $U_\infty \approx 1.72$ (orange dashed lines), as obtained from (4.6) and (4.7) respectively.

which is obtained by balancing viscous damping and gravity in the tangential component of (3.7), and by replacing $\dot{X}_G$ and Δ_{eq} with U_∞ and Δ_∞ in (4.1) respectively. This also leads to a prediction of the associated terminal sliding height:

$$\Delta_\infty = \frac{3^{4/5}}{4} \frac{\kappa^{2/5} \sin^{4/5}\alpha}{\xi^{2/5}\epsilon^{2/5}\cos^{2/5}\alpha}, \tag{4.7}$$

consistent with the scaling relations in (2.7). The convergence to this long-term steady state for the stable sliding case is illustrated by solving (3.7), and the results are depicted in figure 7, showing that the cylinder indeed reaches the terminal velocity and height obtained above.

Naturally, these results are valid as long as Δ remains sufficiently smaller than $\sim\epsilon^{-1}$, so that the lubrication approximation holds. This criterion corresponds to the terminal velocity U_∞ being smaller than $\sim\sqrt{\cos\alpha/\left(\kappa\xi\epsilon^{7/2}\right)}$.

5. Role of poroelasticity

We conclude with a brief discussion of a generalization of our results to the case when the wall is fluid permeable, a problem of some relevance to many biological and geological situations (Biot 1941; Burridge & Keller 1981; Gopinath & Mahadevan 2011), and we follow and generalize the results of Skotheim & Mahadevan (2004*b*, 2005) and Gopinath & Mahadevan (2011) which we summarize below.

We introduce the volume fraction ϕ of fluid in the porous wall, the bulk modulus $\beta^{-1} \gg \mu$ of the solid porous matrix (with μ now being the composite shear modulus of the poroelastic medium), and the isotropic Darcy permeability k, and we note that the pore size $\sim\sqrt{k}$ is small in comparison with the wall thickness h_s. We assume that there is no flow inside the poroelastic wall in comparison with the flow in the lubrication gap, which is valid as long as $kh_s \ll \delta(t)^3$. For example, if $h_s \sim \delta_0$, this follows due to scale separation.

The fluid-permeable wall introduces a new time scale associated with flow-induced stress relaxation given by $\tau_p \sim \eta h_s^2/(k\mu)$, which has to be compared with the lubrication time scale $\tau \sim r\sqrt{\epsilon}/c$ (Skotheim & Mahadevan 2005). If $\tau \gg \tau_p$, the fluid in the wall is in equilibrium with the outside and a purely elastic theory suffices, so that (2.2) is modified to read

$$\delta_s(x, t) = -\frac{h_s(1-\phi)}{2\mu+\lambda}\, p(x, t), \tag{5.1}$$

which simply corresponds to a small effective stiffening due to the presence of a volume fraction ϕ of fluid in the poroelastic wall. In contrast, if $\tau \ll \tau_p$, the pore fluid has no time to adapt and we find that the wall is effectively stiffer, with $(2\mu+\lambda) \to \phi/\beta$, so that

$$\delta_s(x, t) = -\frac{\beta h_s}{\phi}\, p(x, t). \tag{5.2}$$

In both cases there is a purely local elastic response to the driving pressure field. Therefore, all of our previous results directly apply to these limiting poroelastic cases as well, provided that we use the transformations $\kappa \to (1-\phi)\kappa$ if $\tau \gg \tau_p$ and $\kappa \to \beta(2\mu+\lambda)\kappa/\phi$ if $\tau \ll \tau_p$.

6. Conclusions

Using soft lubrication theory and scaling arguments, we have shown that when a cylinder moves freely close to an elastic or poroelastic wall, the flow-induced pressure field exerts a drag force that resists this motion, but it also deforms the wall, which may in turn increase the gap and reduce this drag, as well as create a supplementary lift. This leads to a complex and rich zoology of inertial motions that link sedimentation, sliding and spinning, despite the inertialess motion of the fluid. Indeed, it is the wall elasticity combined with the cylinder inertia that is at the origin of all of these effects, even at low Reynolds number. The striking solutions observed include non-exhaustively oscillations, Magnus-like effect, spin-induced reversal, enhanced sedimentation and long-term steady sliding. While the fully three-dimensional motion of a sphere, or other solid, will have three additional degrees of freedom, we expect many of the qualitative scaling features that we have uncovered to persist.

Appendix A. Zeroth order: the rigid wall

In this first Appendix, we detail the derivation of (3.7) at zeroth order in the dimensionless compliance κ of the substrate. Equation (3.1) is the Stokes equation for the flow, and the no-slip boundary conditions read $U(X, Z=0, T) = 0$ and $U(X, Z=H, T) = \dot{X}_G + \dot{\Theta}$. In addition, the profile of (2.4) becomes

$$H(X, T) = \Delta(T) + [X - X_G(T)]^2\,. \tag{A 1}$$

The corresponding Poiseuille velocity is thus given by

$$U = \frac{P_X}{2} Z\left[Z - \Delta - (X-X_G)^2\right] + \frac{(\dot{X}_G + \dot{\Theta})\; Z}{\Delta + (X-X_G)^2}. \tag{A 2}$$

Then, integrating once the volume conservation of (3.2), with respect to X, leads to

$$P_X = \frac{C + 12X\dot{\Delta} - 12(X-X_G)^2\dot{X}_G + 6(\dot{X}_G+\dot{\Theta})\left[\Delta + (X-X_G)^2\right]}{\left[\Delta + (X-X_G)^2\right]^3}, \tag{A 3}$$

where $C(T) = -(8\Delta\dot{\Theta} + 4\Delta\dot{X}_G + 12\dot{\Delta}X_G)$ is an integration constant, which was identified thanks to the assumed vanishing lubrication pressure P at $X = \pm\infty$. In this case, a second spatial integration leads to

$$P = -\frac{3\dot{\Delta} + 2(\dot{\Theta} - \dot{X}_G)(X - X_G)}{\left[\Delta + (X - X_G)^2\right]^2}. \tag{A 4}$$

The pressure is not an even function in X due to the transverse motion, and therefore there is a tangential drag associated with it, in addition to the normal one. We use (3.4) to evaluate both projections. By parity, the total dimensionless pressure-induced drag force along Z is thus

$$D_{p,\perp} = \int_{-\infty}^{\infty} \mathrm{d}X\, P = -\frac{3\pi}{2}\frac{\dot{\Delta}}{\Delta^{3/2}}. \tag{A 5}$$

Similarly, the total dimensionless pressure-induced drag force along X reads

$$D_{p,\parallel} = -\sqrt{2\epsilon}\int_{-\infty}^{\infty} \mathrm{d}X\,(X - X_G)\;P = \pi\sqrt{2\epsilon}\;\frac{\dot{\Theta} - \dot{X}_G}{\sqrt{\Delta}}, \tag{A 6}$$

which is smaller in magnitude – by a factor $\sim\sqrt{\epsilon} \ll 1$ – than the orthogonal one along Z.

It is important to highlight that we had to go to the next order in $\sqrt{\epsilon}$ to obtain the pressure-induced drag force $D_{p,\parallel}$ in the tangential direction, which is now of comparable magnitude to the tangential drag $D_{\sigma,\parallel}$ obtained from the dominant viscous stress component: $\sigma_{zx} \approx \eta\partial_z u$. Therefore, one has to calculate the latter through (3.5) with $\kappa = 0$:

$$D_{\sigma,\parallel} = -\sqrt{\frac{\epsilon}{2}}\int_{-\infty}^{\infty} \mathrm{d}X\, U_Z|_{Z=H}. \tag{A 7}$$

Using (A 2) and (A 4), it becomes

$$D_{\sigma,\parallel} = -\pi\sqrt{2\epsilon}\frac{\dot{\Theta}}{\sqrt{\Delta}}, \tag{A 8}$$

which precisely compensates the part of $D_{p,\parallel}$ that depends on $\dot{\Theta}$.

Knowing the dominant drag in each direction, one can now study the motion of the cylinder in the presence of gravity and buoyancy. The Z-projection of the balance of linear momentum reads

$$\ddot{\Delta} + \xi\frac{\dot{\Delta}}{\Delta^{3/2}} + \cos\alpha = 0. \tag{A 9}$$

Thus, the sedimentation motion is decoupled from the others. In contrast, the sliding motion is coupled to the sedimentation motion through the X-projection of the balance of linear momentum, as given by

$$\ddot{X}_G + \frac{2\epsilon\xi}{3}\;\frac{\dot{X}_G}{\sqrt{\Delta}} - \sqrt{\frac{\epsilon}{2}}\sin\alpha = 0. \tag{A 10}$$

Finally, the spinning motion can be obtained by the balance of angular momentum which reads

$$\frac{mr^2}{2}\ddot{\theta} = r\;d_{\sigma,\parallel}, \tag{A 11}$$

where the pressure-induced torque is zero since the pressure-induced force acts along a radius of the cylinder. This can be non-dimensionalized as

$$\ddot{\Theta} + \frac{4\epsilon\xi}{3}\frac{\dot{\Theta}}{\sqrt{\Delta}} = 0, \tag{A 12}$$

which results in the trivial non-spinning solution, if $\dot{\Theta}(0) = 0$, due to the absence of driving force. This statement is modified for a soft wall, as studied below.

Appendix B. First-order correction: the soft compressible wall

Here, we detail the derivation of the central system of equations (3.7) at first order in the dimensionless compliance κ of the substrate. Solving (3.1) with the new boundary conditions, $U(X, Z = -\kappa P, T) = 0$ and $U(X, Z = H - \kappa P, T) = \dot{X}_G + \dot{\Theta}$, and the gap profile of (2.4), and conserving the volume of the fluid through (3.2), leads to (3.3). Since $P(X, T)$ depends on X, a direct spatial integration of this equation would lead to an integro-differential equation. We restrict ourselves to perturbation theory in $\kappa \ll 1$, consistent with the assumption of linear elasticity:

$$P = P^{(0)} + \kappa P^{(1)}, \tag{B 1}$$

$$D_{p,\perp} = D^{(0)}_{p,\perp} + \kappa D^{(1)}_{p,\perp}, \tag{B 2}$$

$$D_{p,\parallel} = D^{(0)}_{p,\parallel} + \kappa D^{(1)}_{p,\parallel}, \tag{B 3}$$

$$D_{\sigma,\parallel} = D^{(0)}_{\sigma,\parallel} + \kappa D^{(1)}_{\sigma,\parallel}, \tag{B 4}$$

where both $P^{(0)}$ and $P^{(1)}$ are assumed to vanish at infinity.

Equation (3.3) at zeroth order in κ is equivalent to (A 3), so that the zeroth-order pressure follows from (A 4):

$$P^{(0)} = -\frac{3\dot{\Delta} + 2(\dot{\Theta} - \dot{X}_G)(X - X_G)}{\left[\Delta + (X - X_G)^2\right]^2}, \tag{B 5}$$

while the corresponding zeroth-order drag forces from (A 5), (A 6) and (A 8) are

$$D^{(0)}_{p,\perp} = -\frac{3\pi}{2}\frac{\dot{\Delta}}{\Delta^{3/2}}, \tag{B 6}$$

$$D^{(0)}_{p,\parallel} = \pi\sqrt{2\epsilon}\ \frac{\dot{\Theta} - \dot{X}_G}{\sqrt{\Delta}}, \tag{B 7}$$

$$D^{(0)}_{\sigma,\parallel} = -\pi\sqrt{2\epsilon}\frac{\dot{\Theta}}{\sqrt{\Delta}}. \tag{B 8}$$

Expressing (3.3) at first order in κ then yields

$$\left[\left(\Delta + (X - X_G)^2\right)^3 P^{(1)}_X + 3\left(\Delta + (X - X_G)^2\right)^2 P^{(0)} P^{(0)}_X - 6(\dot{\Theta} + \dot{X}_G)P^{(0)}\right]_X = 12P^{(0)}_T. \tag{B 9}$$

Proceeding as in Appendix A, using three spatial integrations and the abovementioned boundary conditions, one obtains the normal and tangential pressure-induced drag forces as

$$D^{(1)}_{p,\perp} = \frac{45\pi\ddot{\Delta}}{16\Delta^{7/2}} - \frac{63\pi\dot{\Delta}^2}{8\Delta^{9/2}} + \frac{3\pi(\dot{\Theta} - \dot{X}_G)^2}{8\Delta^{7/2}}, \tag{B 10}$$

$$D^{(1)}_{p,\parallel} = \sqrt{\frac{\epsilon}{2}}\left[\frac{23\pi\dot{\Delta}(\dot{\Theta} - \dot{X}_G)}{8\Delta^{7/2}} + \frac{\pi(\ddot{X}_G - \ddot{\Theta})}{2\Delta^{5/2}}\right], \tag{B 11}$$

which are consistent with the steady-state results (Skotheim & Mahadevan 2004*a*, 2005) when $\Delta = \dot{X}_G \equiv 1$ and $\Theta \equiv 0$.

In order to calculate the remaining first-order viscous stress, one expresses the velocity gradient at the surface of the cylinder:

$$U_Z|_{Z=H-\kappa P} = U_Z|^{(0)}_{Z=H-\kappa P} + \kappa U_Z|^{(1)}_{Z=H-\kappa P}, \tag{B 12}$$

where

$$U_Z|^{(1)}_{Z=H-\kappa P} = \frac{P^{(1)}_X}{2}\left[\Delta + (X - X_G)^2\right] + \frac{P^{(0)}P^{(0)}_X}{2} - \frac{(\dot{\Theta} + \dot{X}_G)P^{(0)}}{\left[\Delta + (X - X_G)^2\right]^2}. \tag{B 13}$$

Therefore, using (3.5), one obtains

$$D^{(1)}_{\sigma,\parallel} = \sqrt{\frac{\epsilon}{2}}\left[\frac{\pi(\ddot{\Theta} - \ddot{X}_G)}{4\Delta^{5/2}} + \frac{\pi\dot{\Delta}\dot{X}_G}{2\Delta^{7/2}} - \frac{19\pi\dot{\Delta}\dot{\Theta}}{8\Delta^{7/2}}\right]. \tag{B 14}$$

Finally, the balance of linear and angular momentum leads to the general coupled system of three equations:

$$\ddot{\Delta} + \xi\frac{\dot{\Delta}}{\Delta^{3/2}} + \frac{\kappa\xi}{4}\left[21\frac{\dot{\Delta}^2}{\Delta^{9/2}} - \frac{(\dot{\Theta} - \dot{X}_G)^2}{\Delta^{7/2}} - \frac{15}{2}\frac{\ddot{\Delta}}{\Delta^{7/2}}\right] + \cos\alpha = 0, \tag{B 15}$$

$$\ddot{X}_G + \frac{2\epsilon\xi}{3}\frac{\dot{X}_G}{\sqrt{\Delta}} + \frac{\kappa\epsilon\xi}{6}\left[\frac{19}{4}\frac{\dot{\Delta}\dot{X}_G}{\Delta^{7/2}} - \frac{\dot{\Delta}\dot{\Theta}}{\Delta^{7/2}} + \frac{1}{2}\frac{\ddot{\Theta} - \ddot{X}_G}{\Delta^{5/2}}\right] - \sqrt{\frac{\epsilon}{2}}\sin\alpha = 0, \tag{B 16}$$

$$\ddot{\Theta} + \frac{4\epsilon\xi}{3}\frac{\dot{\Theta}}{\sqrt{\Delta}} + \frac{\kappa\epsilon\xi}{3}\left[\frac{19}{4}\frac{\dot{\Delta}\dot{\Theta}}{\Delta^{7/2}} - \frac{\dot{\Delta}\dot{X}_G}{\Delta^{7/2}} + \frac{1}{2}\frac{\ddot{X}_G - \ddot{\Theta}}{\Delta^{5/2}}\right] = 0, \tag{B 17}$$

which corresponds to (3.7).

REFERENCES

Balmforth, N. J., Cawthorn, C. J. & Craster, R. V. 2010 *J. Fluid Mech.* **646**, 339.

Batchelor, G. K. 1967 *An Introduction to Fluid Dynamics*. Cambridge University Press.

Biot, M. A. 1941 *J. Appl. Phys.* **12**, 155.

Brenner, H. 1962 *J. Fluid Mech.* **12**, 35.

Burridge, R. & Keller, J. B. 1981 *J. Acoust. Soc. Am.* **70**, 1140.

Byun, S., Son, S., Amodei, D., Cermak, N., Shaw, J., Kang, J. H., Hecht, V. C., Winslow, M., Jacks, T., Mallick, P. & Manalis, S. R. 2013 *Proc. Natl Acad. Sci. USA* **110**, 7580.

Campbell, C. S. 1989 *J. Geol.* **97**, 653.

Cawthorn, C. J. & Balmforth, N. J. 2010 *J. Fluid Mech.* **646**, 327.

Davis, R. H., Serayssol, J.-M. & Hinch, E. J. 1986 *Phys. Fluids* **163**, 479.

Dupeux, G., Cohen, C., Le Goff, A., Quéré, D. & Clanet, C. 2011 *J. Fluids Struct.* **27**, 659.

Glenne, B. 1987 *J. Tribology* **109**, 614.

Goldman, A. J., Cox, R. G. & Brenner, H. 1967*a* *Chem. Engng Sci.* **22**, 637.

Goldman, A. J., Cox, R. G. & Brenner, H. 1967*b* *Chem. Engng Sci.* **22**, 653.

Goldsmith, H. L. 1971 *Fed Proc.* **30**, 1578.

Gondret, P., Hallouin, E., Lance, M. & Petit, L. 1999 *Phys. Fluids* **11**, 2803.

Gopinath, A. & Mahadevan, L. 2011 *Proc. R. Soc. Lond* A **467**, 1665.

Grodzinsky, A. J., Lipshitz, H. & Glimcher, M. J. 1978 *Nature* **275**, 448.

Hocking, L. M. 1973 *J. Engng Maths* **7**, 207.

JEFFREY, D. J. & ONISHI, Y. 1981 *Q. J. Mech. Appl. Maths* **34**, 129.
JOHNSON, K. L. 1985 *Contact Mechanics*. Cambridge University Press.
MA, K.-F., BRODSKY, E. E., MORI, J., JI, C., SONG, T.-R. A. & KANAMORI, H. 2003 *Geophys. Res. Lett.* **30**, 1244.
MANI, M., GOPINATH, A. & MAHADEVAN, L. 2012 *Phys. Rev. Lett.* **226104**, 108.
MOW, V. C. & GUO, X. E. 2002 *Annu. Rev. Biomed. Engng* **4**, 175.
MOW, V. C., HOLMES, M. H. & LAI, W. M. 1984 *J. Biomech.* **17**, 377.
ORON, A., DAVIS, S. & BANKOFF, S. 1997 *Rev. Mod. Phys.* **69**, 931.
REYNOLDS, O. 1886 *Phil. Trans. R. Soc. Lond.* A **177**, 157.
SEKIMOTO, K. & LEIBLER, L. 1993 *Europhys. Lett.* **23**, 113.
SEKIMOTO, K. & RABIN, Y. 1994 *Europhys. Lett.* **27**, 445.
SKOTHEIM, J. M. & MAHADEVAN, L. 2004*a* *Phys. Rev. Lett.* **92**, 245509.
SKOTHEIM, J. M. & MAHADEVAN, L. 2004*b* *Proc. R. Soc. Lond.* A **460**, 1995.
SKOTHEIM, J. M. & MAHADEVAN, L. 2005 *Phys. Fluids* **17**, 092101.
SNOEIJER, J., EGGERS, J. & VENNER, C. H. 2013 *Phys. Fluids* **25**, 101705.
TRAHAN, J. F. & HUSSEY, R. G. 1985 *Phys. Fluids* **28**, 2961.
WEEKLEY, S. J., WATERS, S. L. & JENSEN, O. E. 2006 *Q. J. Mech. Appl. Maths* **59**, 277.
WEHBEH, E. G., UI, T. J. & HUSSEY, R. G. 1993 *Phys. Fluids* **5**, 25.